A wireless, 60-channel, AI-enabled neurostimulation platform

Daniel S. Rizzuto[1*†], Zhe Hu[1], Daniel Utin[1], Joshua Kahn[1], Chris Ho[1], Andrew Smiles[1], Robert E. Gross[2], Bradley C. Lega[3], Sandhitsu R. Das[4], Michael J. Kahana[1,4†]

[1*]Nia Therapeutics, Inc., Boston, MA, 02115, USA.
[2*]Rutgers University, New Brunswick, NJ, 08901, USA.
[3*]Department of Neurology and Neurotherapeutics, University of Texas Southwestern, Dallas, TX, 75390, USA.
[4]Department of Psychology, University of Pennsylvania, Philadelphia, PA, 19104, USA.

*Corresponding author(s). E-mail(s): dan@niatx.com;
Contributing authors: zhe@niatx.com; daniel@niatx.com; josh@niatx.com; chris@niatx.com; andrew@niatx.com; robert.e.gross@rutgers.edu; bradley.lega@utsouthwestern.edu; sudas@seas.upenn.edu; mjkahana@niatx.com;
†These authors contributed equally to this work.

Abstract

Electrical stimulation of the human brain has emerged as a powerful therapeutic modality, enabling the alteration of neural circuits underlying cognition and behavior. Recent evidence indicates that stimulation's effects on physiology and behavior depend on endogenous variation in brain state, as measured by field-potential recordings. Here, we describe a 60-channel brain-computer interface – the Smart Neurostimulation System (SNS) – that combines closed-loop analysis of spectral features of the field potential with multi-channel stimulation capabilities. We demonstrate system functionality via bench tests and from an *in vivo* ovine study exercising a subset of the device's functionality. Our ovine study shows that the SNS can reliably measure neural correlates of behavior (motion) and the physiological effects of stimulation. We demonstrate the safety of stimulation via histology following a 120-day stimulation study.

Keywords: brain computer interface, neuromodulation, artificial intelligence, human memory, biomarkers

1 Introduction

Memory loss constitutes one of the major health challenges affecting populations worldwide. Although public attention has largely focused on neurodegenerative diseases of memory, such as Alzheimer's disease, traumatic, infectious, and inflammatory insults to the brain can also cause profound memory loss in otherwise healthy individuals. These latter individuals do not benefit from pharmaceutical interventions that slow the progression of neurodegenerative disorders of memory such as lecanumab[1] and donanemab [2].

Given the profound unmet need facing patients with memory deficits related to acquired brain injury, researchers have investigated electrical stimulation as an alternative therapeutic pathway. Several such studies have obtained promising results. In particular, Ezzyat et al [3] and Kahana et al [4] found that stimulating lateral temporal cortex during predicted memory lapses produced reliable improvements in verbal episodic memory, especially when applying stimulation pulses near white matter tracts with strong functional connectivity to the broader memory network [5]. In these studies, researchers used machine learning models to predict momentary lapses of memory encoding [6], triggering trains of high-frequency (100-200 Hz) stimulation during the predicted lapses.

Technological limitations, however, precluded deploying these therapies in clinical populations as the machine learning algorithms require multi-electrode recordings from widespread brain regions and the use of these recordings to control delivery of stimulation to the brain in a closed-loop system. The aforementioned studies thus relied on the acute evaluation of the algorithms in patients undergoing neurosurgical evaluation for the treatment of drug-resistant epilepsy. However, one can only achieve proof of concept in these research studies. Determination of whether closed-loop stimulation constitutes a viable chronic therapy for individuals suffering from memory loss awaits the development of combined hardware and software systems that can decode mnemonic variability and trigger stimulation chronically during everyday life. The present paper describes progress towards developing a wireless, 60-channel AI-enabled brain-computer interface, which we call the Smart Neurostimulation System, or SNS.

2 The Smart Neurostimulation System (SNS)

Figure 1 illustrates the overall system design. The SNS includes four custom-designed depth leads for sensing and stimulating neural tissue; a cranially-mounted implantable pulse generator (IPG) for processing neural data and controlling therapy delivery; a wearable External Processor (EP) that provides power to the IPG and acts as a communication hub; and a physician Programmer and cloud-based AI platform that is used to personalize the therapy for each patient.

To create the personalized therapy, we ask patients to perform repeated memory tasks in which they study and subsequently recall lists of common words (this is a standard method used in neuropsychological assessments of memory function). The SNS records multi-channel field potentials during each phase of the memory task. Applying a spectral filters to the time series of EEG data allows the IPG to estimate LFP power at frequencies ranging from 3 to 180 Hz. Using machine-learning methods, we train models to predict mnemonomic success using the pattern of spectral power estimated across frequencies and channels. Applying these models to data from unseen holdout sessions determines how well the model can predict variability in memory performance, providing a rapid readout of mnemonic function at any given time. We illustrate these methods in Figure 1f,g.

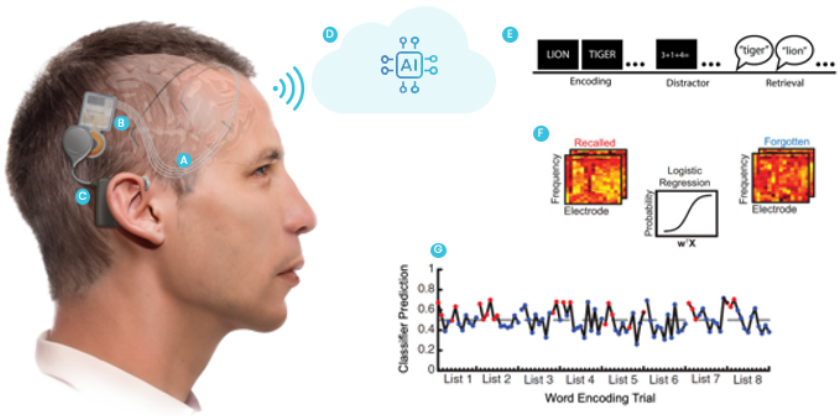

Fig. 1 The Smart Neurostimulation System. Depiction of the SNS installed in an artist's rendering of a typical patient. The SNS includes: (a) four depth leads with 64 contacts; (b) a cranial Implant responsible for neural sensing and stimulation; (c) a wearable External Processor providing power and acting as a communications hub; and (d) a cloud-based AI platform to personalize the therapy for each patient. To predict momentary memory lapses, researchers record from multiple electrodes in widespread regions while subjects study and recall word lists (e). Multivariate classifiers (penalized logistic regression) learn a mapping between the distribution of spectral power across electrodes and the subsequent recall status of encoded items (f). Such models can predict, in hold out sessions, which list items subjects will remember (red dots) or forget (blue dots) (g). The SNS uses these models to trigger stimulation during predicted memory lapses and to optimize stimulation parameters.

Figure 2 shows the prototype IPG, Depth Leads, and External Processor. The IPG senses local field activity from 60 electrodes (plus four reference electrodes), processes the resulting neural data and controls therapy delivery. The External Processor (EP) contains a rechargeable battery and provides power to the IPG via an inductive link. The inductive link between the IPG and the EP has a 2.2 Mbps data rate, which

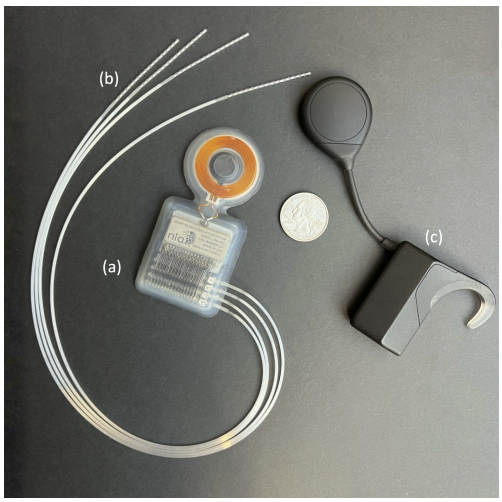

Fig. 2 The Smart Neurostimulation System prototype, including: a) the implantable pulse generator; b) four depth leads containing up to 16 electrodes each; and c) the external processor. All device materials were selected for biocompatibility and history of usage within medical devices. The IPG is fully encapsulated in silicone. It includes a hermetically-sealed titanium can surrounding the embedded electronics, platinum/iridium, stainless steel and pellethane in the lead connector assembly, and Parylene-C surrounding the gold-coated magnet. The depth lead utilizes platinum/iridium electrodes, a stainless-steel set screw block, and a pellethane lead body. EP materials include ABS plastic, nylon and silicone. A quarter is included for scale.

is sufficient bandwidth to stream 1000Hz local field potential data from all 60 electrodes to the EP. Bench-top testing of the inductive link demonstrates reliable data transmission across scalp distances ranging from 4 to 10mm.

The EP also acts as a communication hub between the hardware and software components of the system, providing USB for high-speed communication to the Programmer and Bluetooth low energy (LE) for low-bandwidth communication with a mobile phone app. The SNS authenticates and encrypts all communications end-to-end using 128-bit AES-GCM, ensuring only authenticated users and devices can connect to the device, and preventing the administration of malicious therapy parameters. Like a cochlear implant, the EP is intended to be recharged overnight, when therapy delivery is not required.

The design of the SNS arose from a need to meet multiple simultaneous constraints. Specifically, we needed a device that could record field potentials from >32 electrodes in widespread brain locations at sampling rates greater than or equal to 500 Hz (to discern high-frequency correlates of variable memory function [8**?**]), and the ability to rapidly deliver bursts of electrical stimulation in response to predicted memory lapses, derived from machine-learning / AI models trained on data sampled from the device. Furthermore, we sought to design a cranial implant of a similar size to those proven safe in prior applications, such as the Neuropace RNS.

In our prior studies, our team has demonstrated the ability to improve human memory by responsively stimulating neural circuits within 200 ms of an identified memory lapse event [3, 5]. These studies utilized bursts of bi-phasic square wave pulses

at frequencies between 50 and 200 Hz, amplitudes of 0.1 to 3 mA, and durations of 250 to 1 sec. These stimulation parameters, along with the requirements of recording using a 500 Hz sampling rate from all channels, and evaluating brain state eight times per second, determines the power requirements of the neurostimulation therapy. We estimate that a device with these capabilities uses up to 25mW total power. To deliver therapy for 12 hours between charges, requires an implanted battery with capacity of 75mAH. To minimize the burdens of daily implant recharging, and battery replacement surgery every three years, we decided to use an externalized battery, worn on an EP (Figure 2), which provides inductive power to the implant in a similar fashion to a cochlear implant device. Externalizing the battery required expanding its capacity to offset inductive power loss and the EP's power usage. The resulting EP battery has a capacity of 315 mAh to support approximately 12 hours of use. We expect the device's power efficiency to continue to improve as clinical development advances.

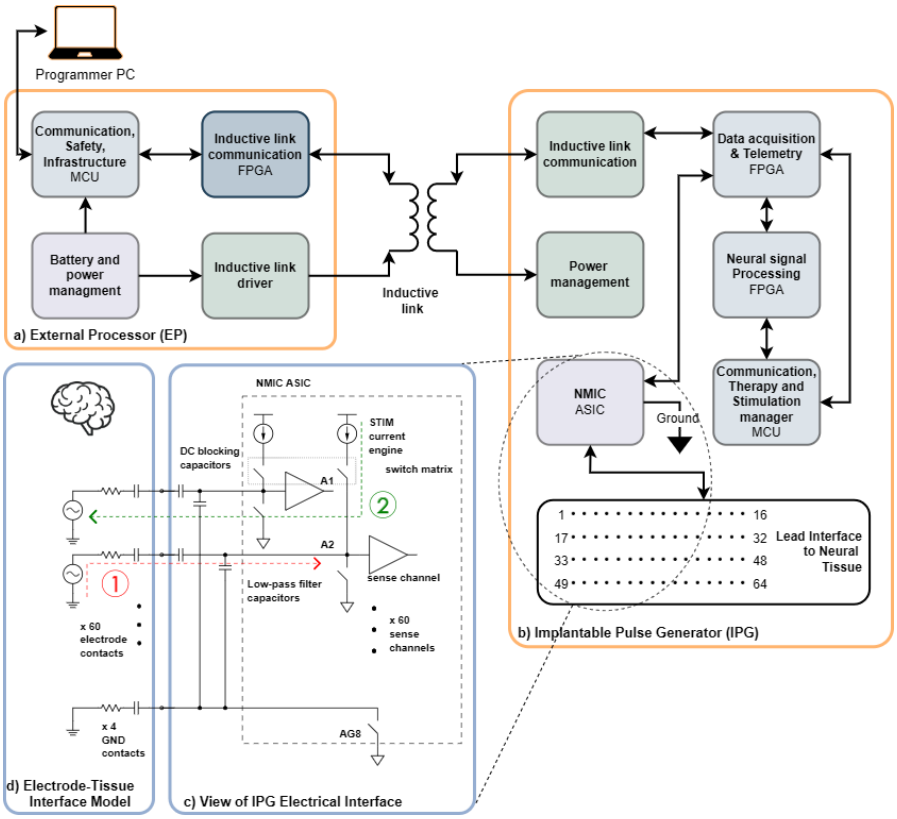

Fig. 3 The SNS system hardware and electrical interface schematic. a) the External Processor (EP), and b) the Implantable Pulse Generator (IPG). c) Expanded view of the electrical interface between the stimulation/sensing ASIC (Neuromodulation Integrated Circuit; NMIC) and the leads. d) the Electrode-Tissue interface model. Information (data or commands) can be sent via the EP (a) to the IPG (b) and in reverse. The IPG records neural data via (c) and transmits it to the EP (which can then communicate with an external program (PC). The electrical interface and Electrode-Tissue interface (c) and (d) illustrates both sensing (1) and stimulation (2) circuit models.

Figure 3 describes the hardware architecture of the SNS system. The EP (a) and IPG (b) interact via an inductive link composed of two conductive coils, allowing wireless power and data transmission. Command and response data flow bidirectionally through this link, while neural data are transmitted in parallel from the IPG to the EP. Once the neural data arrive at the EP, they can be sent to a PC over USB or to a mobile phone via Bluetooth LE. A microcontroller (MCU) in the EP controls most of the system logic, including communication, safety systems, and firmware updates. A field programmable gate array (FPGA) controls the inductive link communication protocol on both the EP and the IPG. On the IPG, power is received over the inductive link and regulated by power management hardware, while an MCU processes all communication messages and manages therapy safety.

Figure 3.c) illustrates the electrical interface between the IPG hardware and the neural tissue. The IPG lead interface holds four leads with 16 electrodes each. Sixty of the 64 Platinum-Iridium electrodes can sense and stimulate neural tissue; the remaining four electrodes, one on each lead, serve as electrical references. On the IPG, a proprietary NeuroModulation Integrated Circuit (NMIC) chip connects to the electrode contacts through DC-blocking capacitors. This custom Application-Specific Integrated Circuit (ASIC) was designed specifically for brain interfaces to provide sensing and stimulation capabilities[9, 10]. Inside the NMIC, there are 64 independent sensing and stimulation channels, one for each electrode contact.

We model the interface between the brain and the NMIC, which records neural activity, as an R-C circuit. Filtering capacitors on the IPG circuit board shunt noise to ground contacts. Sense channels continuously sample neural signals at 1000Hz, referenced to GND contacts. The IPG transfers neural data for all channels together at 1000 Hz to the EP (via inductive link) which transmits to a PC (over a wired USB connection). The NMIC also streams a copy of the data to a local FPGA for online processing and analysis (see description of Figure 4).

The IPG is designed to deliver biphasic, square-wave, stimulation pulses in a bipolar configuration through two electrodes located on the same lead. During stimulation, the NMIC stimulation driver first sources current through the selected anodic electrode while sinking current through the selected cathodic electrode. The role of these electrodes is reversed during the second phase of the pulse.

Figure 4 shows the firmware implementation of the SNS system and its major roles of sensing brain activity and making therapy decisions. The firmware ensures proper functioning of the EP and IPG devices and includes multiple programs running on microcontrollers (MCUs) and Field Programmable Gate Arrays (FPGAs). The firmware supports communication for command and control, battery management, firmware updates, event logging, and other features. Its main therapeutic tasks are transmission of neural data and therapy application.

The firmware can transmit neural data from the IPG through the EP to an external PC, supporting offline analysis and therapy personalization (see *Streaming Path* Figure 4). In this configuration, neural signals are sensed by the IPG, then collected and forwarded (Figure 4.a) over the inductive link to the External Processor (Figure 4.b), which tags the data and sends it via USB to a PC computer, where it is stored for offline analysis. This path is independent of therapy administration.

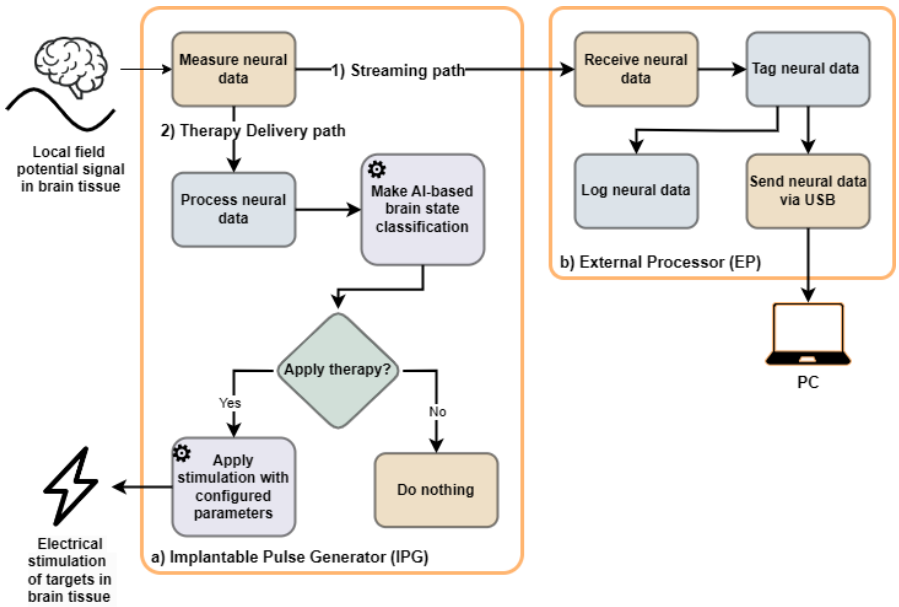

Fig. 4 SNS firmware overview. The SNS includes firmware running on both the IPG (a) and the External Processor (b) to sense neural data and administer electrical stimulation. Once it is sensed from the brain, neural data can take two paths (numbered): 1.) a Streaming path where data is sent to an external computer via USB; and 2.) a Therapy Delivery path where the data are processed and therapy is administered based on brain state classification. Brain state classification and therapy delivery blocks are programmable and adaptable (marked with a gear icon).

In day-to-day operation, the IPG senses neural data, classifies the brain's state, and decides whether to apply stimulation. This is shown in Figure 4 as the Therapy Delivery path. In this pathway, data are periodically processed within the FPGAs (Figure 4.a) to estimate the spectral power within multiple frequency bands in a given time window. These processed data are used by a classifier in the MCU to make a therapy decision based on a configured set of parameters determined by individualized AI-based training. If the brain state classifier indicates that therapy should be applied, the IPG applies electrical stimulation to the brain. The parameters of this stimulation include the target electrode, amplitude, pulse width, and duration. The brain state classifier and stimulation parameters are highly configurable.

3 Preclinical Ovine Study

Following approval from the local IACUC, a functional neurosurgeon (R.E.G.) implanted the IPG, one 8-channel SNS depth lead and one off-the-shelf DBS lead (Medtronic 3387S-40) in a female Polypay sheep (aged 16 months; body weight = 60.3kg at implantation and 70.5 kg at end of study). Following surgery, the sheep recovered for six days before we initiated neural recording and stimulation. Throughout the study, the sheep could move freely (untethered) in their pen under the care of a licensed veterinarian.

We recorded neural activity and applied brain stimulation between Days 7 and 120 of the study. The animal was sacrificed at study exit and histology was performed to evaluate the effects of the device materials and electrical stimulation on the surrounding neural tissue, which showed no adverse reactions to either lead. Figure 5 illustrates the study design and surgical approach and shows the location of the electrodes in each hemisphere.

Non-contrast computed tomography (CT) scans were collected during procedure planning (Day -7), following device implantation (Day 0), and prior to study exit (Day 120). Bright metal artifact on the post-surgical and study exit scans helped to visually identify and localize the electrodes. Excessive artifact creates diffuse signal that makes localization more difficult, so we used the iterative metal artifact rejection (iMAR) algorithm during scanning to minimize this.

The post-surgical CT scan was semi-automatically aligned with the Turone sheep brain MR atlas [11, 12] using the ITK-SNAP software. The study exit CT scan was also semi-automatically aligned with the post-surgical CT scan using the ITK-SNAP software. The two CT scans were then re-sliced to the template image and visualized in ITK-SNAP along with the anatomical regions in the atlas as overlays for annotation and localization. Using metal artifacts on CT we identified the (approximate) 3D coordinates of the electrode contacts. Anatomical locations were read from the sheep atlas label overlay. Localizations for the post-surgical and study exit CT scans were done independently and compared post-hoc to measure lead migration.

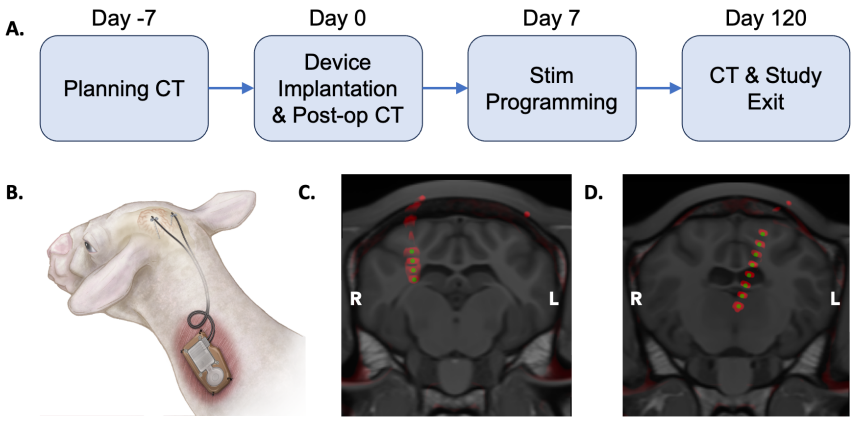

Fig. 5 Preclinical study design and surgical approach. (A) Time course of the preclinical study. CT imaging was collected on Day -7, Day 0 (post-implantation) and Day 120 (prior to study exit). (B) Illustration of the implanted device. The IPG and a protective exoskeleton were implanted into a pocket in the neck, and two leads were implanted into the left and right parietal lobes. (C) CT imaging showing the locations of the control electrodes implanted in right hemisphere. (D) CT imaging showing the locations of the SNS electrodes implanted in left hemisphere.

Table 1 shows the anatomical locations of all monopolar electrodes in the brain. All eight of the SNS electrodes were used for the study (labels N1 through N8), while

only three of the electrodes from the off-the-shelf control lead were used (labels M1 through M3), as one contact was used for mechanical fixation of the lead to the IPG. Bipolar "virtual" electrode recordings were derived from the monopolar recordings prior to analysis. Table 2 shows the midpoint of each virtual bipolar pair(e.g., virtual electrode N1-N2 was derived from monopolar electrodes N1 and N2). In addition to creating virtual bipolar electrodes from the nearest neighbor monopolar electrodes, we also created a virtual electrode between the first and last electrode on each lead (e.g., N8-N1).

Table 1 Monopolar electrode locations at end of study.

Electrode label	X	Y	Z	Anatomical Label
N1	-0.5	5.5	2	Nucleus intermediodorsalis, left
N2	-1.75	5.5	6	Nucleus habenulae, left
N3	-2.75	5.5	8.75	Fornix, left
N4	-4	6	12	Lateral ventricle, left
N5	-5	6	15.25	White matter bundle, left
N6	-6	6	18.25	Lateral gyrus, left
N7	-6.75	6.25	21.5	White matter bundle, left
N8	-8	6.25	25	White matter bundle, left
M1	13.25	-1.25	10	White matter bundle, right
M2	13.75	-1.25	12.5	Caudate, right
M3	14.25	-1.25	15.25	White matter bundle, right

See text for a description of electrode localization methods.

Table 2 Bipolar "virtual" electrode locations at end of study.

Electrode label	X 2	Y	Z	Anatomical Label
N1-N2	-1.125	5.5	4	Nuclei paraventricularis thalami, left
N2-N3	-2.25	5.5	7.375	Third ventricle
N3-N5	-3.875	5.75	12	Lateral ventricle, left
N5-N6	-5.5	6	16.75	White matter bundle, left
N6-N7	-6.375	6.125	19.875	Lateral gyrus, left
N7-N8	-7.375	6.25	23.25	Ectolateral gyrus, left
N8-N1	-4.25	5.875	13.5	lateral ventricles, left
M1-M2	13.5	-1.25	11.25	White matter bundle, right
M2-M3	14	-1.25	13.875	White matter bundle, right
M3-M1	13.75	-1.25	12.625	Caudate, right

See text for a description of electrode localization methods.

4 Neural Recordings and Stimulation Performance

The SNS samples multi-channel EEG signals at 500 Hz and generates charge-balanced square-wave stimulation pulses on any pair of electrodes with a range from $0.02-5mA$ pulse amplitude, $15-500\mu s$ pulse width, and $14.7-256Hz$ pulse frequency. Stimulation

trains are unlimited in duration and may be bipolar-biphasic or monopolar-biphasic. In our preclinical pilot, we used two electrodes: an off the shelf four-channel DBS lead (Medtronic Model **3387S-40**) and a custom 8-channel lead utilizing industry-standard materials (Platinum/Iridium electrodes and pellethane lead body), manufactured by Nia Therapeutics.

To evaluate the effect of brain stimulation on neural recordings, we varied stimulation parameters across multiple sessions and days to evaluate the effect of stimulation amplitude and frequency on the neural signals recorded on nearby electrodes (see *Methods*). During this experiment, we applied 300 μs biphasic stimulation pulses at frequencies of 25, 50, 100 and 200 Hz and amplitudes of 0, 200, 400, 600, 800, and 1000 μA across a bipolar pair of neighboring electrodes ($N5 - N6$) located in left hemisphere white matter (see Figure 5D). The experiment generated 30 trials of each of the 24 frequency $\times$ amplitude combinations. We shuffled the order of stimulation *trials* to create 10 uniquely ordered session protocols that minimized trial order confounds. As illustrated in Figure 7A, each trial applied stimulation for 500 ms, with a random delay of $2000-2250ms$ (uniformly distributed) between the offset and onset of consecutive stimulation trials. Overall, we collected a total of 41 sessions of 720 trials each from our single subject (for a total of 29,520 trials). We chose to reject any trial with $\geq$ 10ms of data loss in the pre- or post-stimulation recording window, resulting in 304 ($\approx$1%) excluded trials.

Two electrodes, one on each lead (N4 and M1; see Table 1) were electrically shorted together and served as the electrical reference for all electrode recordings. Bipolar referencing, computed as the voltage difference between pairs of adjacent electrodes, filtered out signals common to both channels. This referencing scheme attenuates oculomotor and electromyographic artifacts that can mix with neural signals, and large-N human studies have shown that bipolar referencing of intraparenchymal electrodes better resolves the neural correlates of memory [13].

The inductive communication obviates the need for line noise filtration. However, communication over the inductive link can fail from momentary displacement of the coils. Communication failures lasting $> 10ms$ occurred on approximately 1% of trials; we excluded these trials from our analyses. An additional source of artifact arises as charge dissipates exponentially post-stimulation with a halftime of approximately $1000ms$. Spectral leakage from this decay has negligible impact on frequencies of interest in our analysis, which occur above $3Hz$.

To measure the effect of stimulation on neurophysiology, we extracted intracranial EEG signals recorded during the 750ms preceding and following each stimulation train at each of the six bipolar electrode pairs on the SNS lead. We then used Welch's method, based upon the fast-Fourier transform, to calculate the power spectral densities during the pre-stimulation and post-stimulation periods, as illustrated for a representative trial in Figure 7B. Prior to further analysis, we computed the log-transform of each power value, as in previous work [8, 14]. For each frequency f we computed the difference in post- and pre-stimulation power as $\Delta_{\mathrm{P(f)}} = \mathrm{P(f)}_{post} - \mathrm{P(f)}_{pre}$ (Figure 7C).

The present parameter search experiment sought to establish that the SNS can successfully modulate post-stimulation neural activity. We thus asked whether our

neuromodulatory index, Δ_{power}, reveals consistent changes for at least some electrode-frequency pairs. Our analysis approach builds on a prior parameter search study [15] in humans. They demonstrated increased high-frequency activity in the post-stimulation period, with this effect being strongest when stimulating at 200 Hz as contrasted with lower-frequency stimulation trains. Prior research in both human and non-human animals has shown that HFA increases correlate with increases in neural firing rate, thus linking stimulation-related spectral changes to the modulation of neural activity.

Consistent with prior work [15], we found that 200 Hz, 1 mA stimulation generally increased high-frequency activity at nearby recording electrodes (see Figure 7D). Next, we examined how Δ_{HFA} varied as a function of stimulation amplitude and frequency at each of the six bipolar electrode pairs. As shown in Figure 7 we found that both increasing stimulation amplitude and increasing stimulation frequency increased HFA in the poststimulation period. This extends prior work [15] and demonstrates the dual stimulation and recording functionality of the SNS.

In sham and some low amplitude conditions, we found small but significant decreases in alpha power at some electrodes. The curios decrease in power in the sham condition likely reflects carryover effects from prior stimulation events. This is because most sham trials followed stimulation trials.

5 Multivariate Classification of Movement

We next asked whether signals recorded by the SNS could predict changes in the animal's behavioral state. To this end, we recorded data on the animal's activity level, gauged by a three-dimensional accelerometer attached to the animal's neck. We recorded acceleration for each of the cardinal axes at 10 Hz during seven two-hour daytime sessions over two weeks. When the accelerometer sample magnitude exceeded a threshold value of $0.03m/s^2$, we labeled it "movement." Otherwise, we labeled it as "stillness." We then applied a further criterion to assign labels to sustained periods of movement or stillness. Specifically, we counted the number of "movement" samples in a 10-second sliding window across all labeled samples and created a "high activity" event if the count exceeded 27. "low activity" events were created by finding all spans of at least 600 "stillness" samples before the event and 150 "stillness" samples after the event. These values were selected to produce 150 to 250 events per typical 2-hour recording session. Applying this secondary criterion resulted in periods of movement, periods of stillness, and non-labeled periods of ambiguous accelerometer readings.

We included data collected in the recorded sessions as input to a L^2-penalized logistic regression classifier trained to discriminate brain activity predictive of whether the animal is moving or still. We used spectral power averaged across the time dimension for each "movement"/"stillness" event epoch ($0 - 1,000ms$ relative to the event onset) as the input data. Thus, the features for each observed individual "movement"/"stillness" event were the average power across time, at each of the eight analyzed frequencies $\times N$ electrodes. We used L^2-penalization, setting the penalty parameter (C) to 2.4×10^{-4} based on the optimal penalty parameter reported by Ezzyat et al. (2018). We then computed the areas under the ROC curve (AUC value)

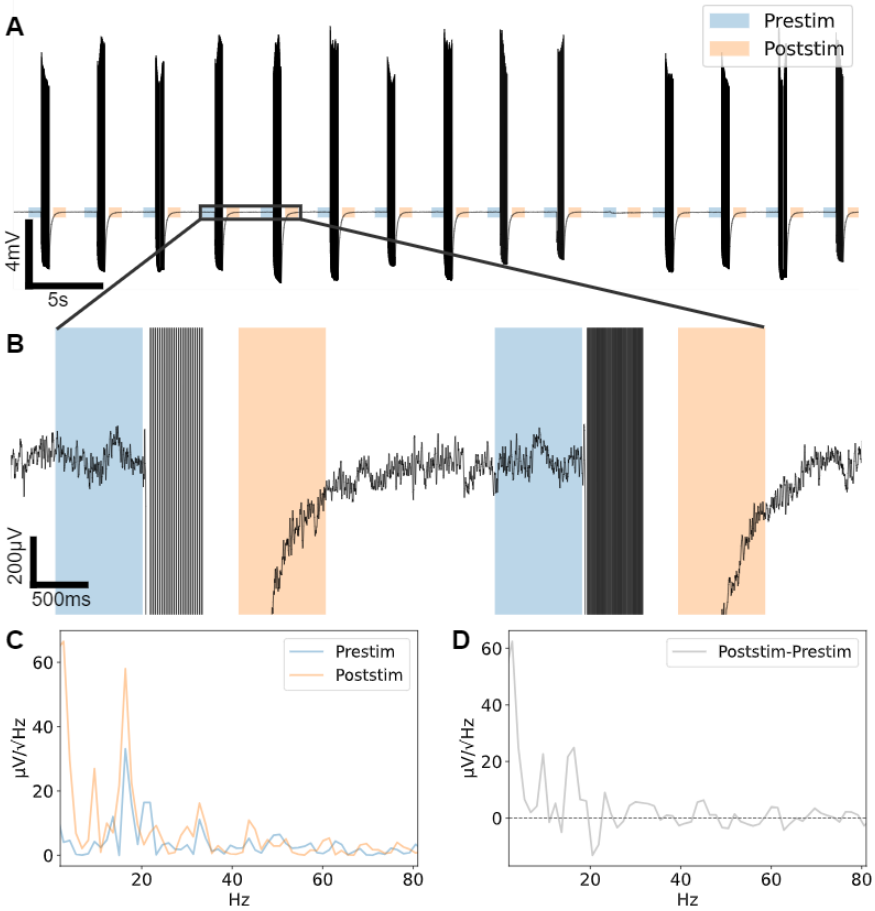

Fig. 6 Parameter Search Methods and Example Data. A. Example field potential recorded from a bipolar electrode pair (N5-N6) during one of the 41 experimental sessions. The SNS delivered 500 ms bi-phasic stimulation bursts at varying frequencies [f = 25, 50, 100 and 200 Hz] and amplitudes [Sham, 200, 400, ..., 1000 μA]. Each parameter combination occurred thirty times (randomly ordered) across a single parameter search session. B. Enlarged view of two stimulation trials with regions demarcated to illustrate our analyses' 750 ms prestimulation and poststimulation intervals. C. Sample power spectral densities (PSDs) for the pre- and post-stimulation intervals. D. To evaluate the physiological effects of stimulation, we compared spectral power in these intervals at each frequency.

to quantify classifier performance. AUC measures a classifier's ability to identify true positives while minimizing false positives, where chance $AUC = 0.50$.

We assessed classifier performance using a leave-one-session-out (LOSO) method where, for each holdout session, we built a classifier based on the remaining sessions and then used it to predict event outcomes of the holdout session. The AUC was then calculated based on aggregated labeled/predicted outcomes for all holdout sessions.

Panel A shows the results of cross-validation in an example two-hour session. Red dots represent events labeled as "movement," whereas blue dots represent events

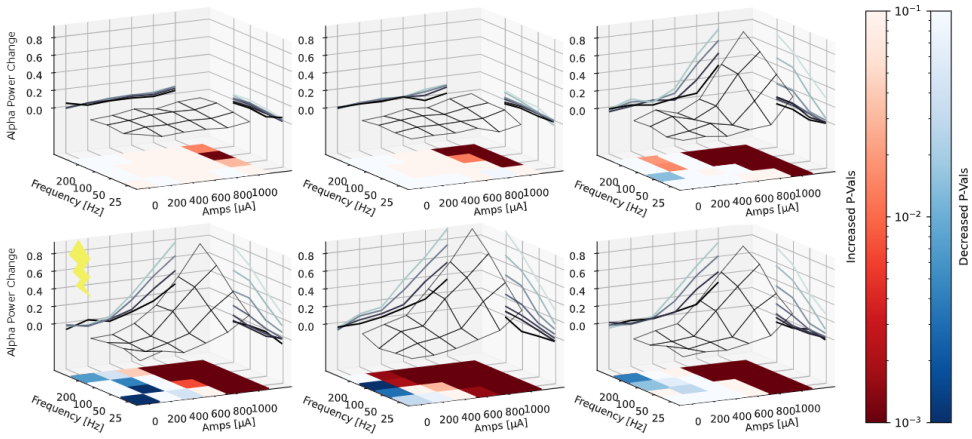

Fig. 7 Stimulation's Physiological effects. A. We illustrate the effect of stimulation on alpha frequency (10Hz) activity in each of the six bipolar electrode pairs (N1-N2 top left, N6-N7 bottom right). The yellow bolt indicates the stimulated pair (N4-N5). Across most channels, higher amplitudes and frequencies resulted in greater stimulation-related power increases.

labeled as "stillness." We derived these labels using the motion detection algorithm described above. Periods that neither met our criteria for movement nor stillness have any dots.

Accelerometer readings, shown as cyan bars, suggest that during this two-hour interval, the animal exhibited three periods of significant movement activity and two periods of reliable stillness, as indicated by the corresponding blue and red dot clusters. Panel A shows that blue dots tend to fall under the 0.5 classifier output threshold, and red dots tend to stay above it, indicating that classifier predictions agreed with the accelerometer reading interpretations in most cases.

To quantify model performance, we illustrate the classifier's hit rate (classify high activity as high) and false alarm rate (classify low activity as high) as a function of the criterion value. To the extent that the ROC curve rises above the positive diagonal line connecting $(0, 0)$ and $(1, 1)$ the model generalizes from the training to the test data, predicting periods of activity from spectral EEG features. To the extent that neural features reliably classify the animal's activity in holdout sessions, we will find a high hit rate even when we have a relatively low false alarm rate. Indeed, we find that the curve rises quickly towards 1.0 as the false alarm rate increases, suggesting excellent classification of holdout data. The area under the ROC curve (AUC) quantifies classification performance. Averaging across seven holdout sessions, we observed an average AUC value of $0.952 \pm 0.005 SEM$. We can compare the true ROC curves to those created by applying the same classification model to data with permuted labels (shuffling labels across the events within each session). This "null" ROC curve appears as the gray curve in Figure 2B.

Previous analyses of neural data during motor tasks have identified a specific pattern of spectral power associated with movement. Specifically, during and immediately preceding movement, researchers have found increases in high-frequency power (> 30

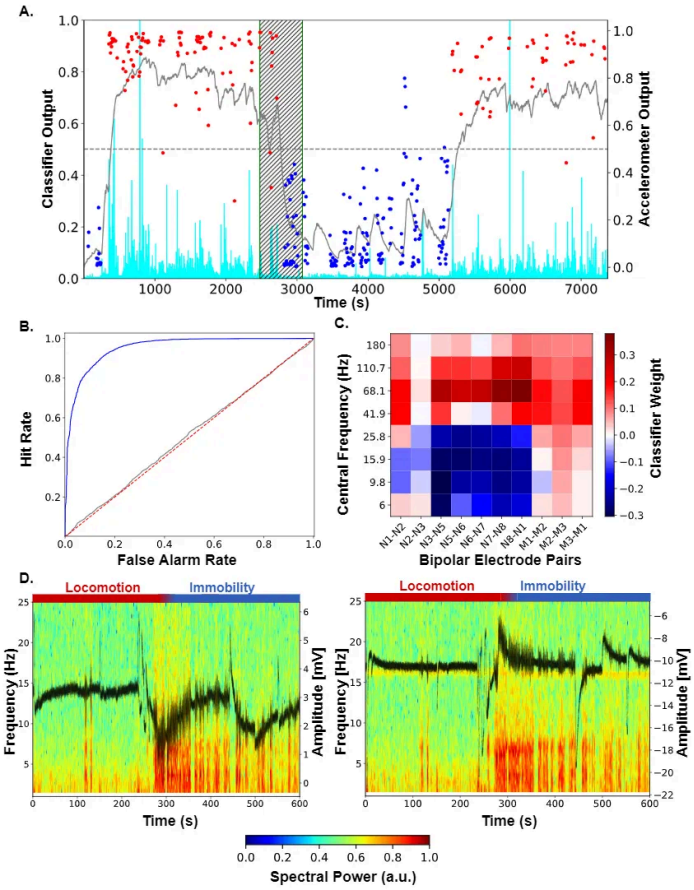

Fig. 8 Classification of animal movement. A. We trained an L2 logistic regression classifier to predict periods of movement vs. stillness based on spectral features extracted from 10 bipolar electrode pairs (Methods). Across a two-hour hold-out session, we show that classifier output probability (gray) tracks periods of movement (red) and stillness (blue). These representative periods were chosen based on the accelerometer magnitude readings (cyan) sampled at 10Hz and high-pass filtered with a cutoff at 0.1Hz. B. A ROC analysis, which shows the relation between true and false positives as a function of decision criterion, quantifies classifier performance in hold-out sessions. This analysis revealed an Area Under the ROC (AUC) of 0.952 $\pm$ 0.005 (gray line shows the same relation for randomly permuted data). C. The Haufe method reveals the degree of influence of different features on classification performance while adjusting for the covariance structure in the model. Here we see that increased weights on high frequencies (red-colored squares) and decreased weights on low frequencies (blue-colored squares) predicted movement. This pattern mirrors findings from primate studies, where increases in high-frequency and decreases in low-frequency activity track a variety of motor and cognitive operations. D. Spectral plots of the shaded interval in panel A, with overlaid time series, show increases in low-frequency power following the animals transition from locomotion to immobility (electrode pairs N5-N6, left, and N6-N7, right).

Hz) and decreases in low-frequency power (see Burke et al., 2015, for a review). To determine whether our logistic regression classifier uncovered similar neural correlates of movement, we applied the Haufe method [16] to the weights obtained from the optimal classifier fit to all seven sessions. This method transforms classifier weights to account for the covariances between features. Here, we find that across most bipolar recordings, increased high-frequency power (squares with red shading) and decreased low-frequency power (squares with blue shading) marked high activity periods.

6 Discussion

Direct electrical brain stimulation has emerged as a therapy for wide-ranging neurological and psychiatric disorders, including Parkinson's disease and essential tremor [17] and more recently, intractable epilepsy [18] depression [19] and obsessive-compulsive disorder [20]. With the exception of responsive stimulation for the treatment of epilepsy, other neurostimulation devices lack the ability to administer stimulation depending on brain state; more typically, stimulation occurs at regularly timed intervals independent of the state of the brain. Another class of emerging technologies aims to sense multi-channel brain activity for decoding purposes. Such devices may help treat patients with motor-neuron disease, spinal cord injury, or stroke, by detecting intended motor functions and controlling a neural prosthesis [21–24].

Here, we describe the Smart Neurostimulation System (SNS), a device that can sense brain signals to detect momentary changes in brain function. These decoded signals determine when, where, and how to apply electrical stimulation. The SNS has 64 electrodes on four leads, and is able to simultaneously measure electrical fields across 60 bipolar contacts (four electrodes serve as reference channels, one on each lead). The ability to both sense and stimulate the brain in a closed-loop system may be particularly useful in applications to neurocognitive and affective disorders where functional impairments can vary dramatically from moment to moment and day to day [25]. As a proof-of-concept for such a therapy, Ezzyat and colleagues [3, 5] found that stimulating the lateral temporal cortex during predicted memory lapses produced significant memory improvements in a sham-controlled, double-blinded study involving patients who had electrodes implanted for the treatment of pharmacoresistant epilepsy. Kahana et al. found similar memory gains in a memory-impaired cohort of epileptic patients with a history of moderate-to-severe traumatic brain injury [4]. By training logistic regression classifiers on spectral activity measured during learning, these authors could reliably predict which studied items would be subsequently recalled or forgotten. They then evaluated whether triggering stimulation on predicted memory lapses could acutely benefit memory. Ezzyat et al (2023) further showed that mnemonic benefits only appeared for closed-loop stimulation (random stimulation did not improve memory).

We designed the SNS to deliver closed-loop stimulation chronically via an AI-enabled brain implant (IPG) that communicates wirelessly with an external processor (EP). The EP is designed to be worn on the ear, similarly to a cochlear implant sound processor. The EP also delivers power inductively to the IPG via a rechargeable battery and acts as a communication hub between the IPG and the cloud-based AI platform.

Clinical programmer software, designed for future human studies, will allow the SNS to receive programming from patient-specific models of variable function. These models will trigger therapeutic stimulation, altering physiology based on variability in a particular patient's brain state. In the case of memory, predicted memory lapses will trigger stimulation, and classifier decoded memory output will allow for optimization of stimulation parameters.

The Neuropace RNS represents the closest predicate to the SNS. Like the SNS, the RNS can record field potential and stimulate the brain in closed loop, and both systems possess onboard signal processing functions. However, unlike the SNS, which can record from 60 channels (bipolar electrode pairs) in four separate brain regions, the RNS can record from a maximum of six channels in two brain regions. Because seizures often localize to a small region of the brain, the six channels of the RNS have proven adequate for controlling seizures, or at least significantly reducing seizure frequency, in many patients. However, memory-related brain signals occur across a distributed network of brain regions [6, 26] and, as such, require the widespread surveillance capabilities of the SNS and the ability to adaptively select among a larger set of stimulation targets. Analyses of large open-data sets [27, 28] informed the SNS design by identifying whole-brain patterns of neural activity that signal periods of good and poor memory.

To exercise the basic capabilities of the SNS we report a preclinical study in an ovine model. Owing to the small size of the sheep brain, we implanted two multi-contact depth leads: an 8-electrode lead designed specifically for the SNS IPG and a commercially-available 4-electrode lead (Medtronic Model 3387S-40). Applying stimulation at a single pair of contacts on the SNS lead demonstrated that increasing stimulation amplitude and frequency systematically alters neural activity (alpha power) at the other recording electrodes. Further, we demonstrate that personalized logistic regression classifiers, trained on recording of neural data from all electrodes, reliably predicted animal movement in hold out sessions. These results demonstrate *in vivo* that the SNS can detect and modulate behaviorally relevant neural signals. Histological analyses show no adverse tissue response to the SNS lead (or the Medtronic control lead).

Limitations and Future Design Considerations

Although 60 channels have proven sufficient to reliably decode memory lapses in analyses of large open datasets [13, 29], increasing the number of channels would improve classifier performance and thereby improve parameter optimization and stimulation timing. Whereas we can imagine designing chronic leads with higher spatial sampling, increasing the number of leads much beyond four would increase the risk of bleeds, the surgical procedure's complexity, and the size of the IPG. The architecture of the SNS could readily accommodate a doubling of the channel count, with the major impediment being the size of the connector block necessary for mating the leads with the IPG.

Conclusions

The Smart Neurostimulation System (SNS) presents an innovative leap in neuromodulatory technology, offering simultaneous 60-channel brain activity monitoring and automatically configurable, targeted electrical stimulation based on real-time spectral analysis of neural data. In a preclinical study, the system demonstrated the ability to modulate alpha-band power in response to stimulation. This modulation aligns with previous findings from acute human stimulation studies [15]. Furthermore, the SNS's capacity to decode behavioral states from neural signals and predict motor activity validates its functionality beyond simple neural modulation. The ovine model study confirms the system's efficacy in both recording and stimulating the brain with high spatial resolution, underscoring the potential for future clinical use in addressing memory impairments. This advancement opens the door for chronic, personalized neuromodulation therapies that adapt to individual variability in brain states, a critical need for patients suffering from diverse cognitive and neurological deficits.

Supplementary information. N/A

Acknowledgements. N/A

Declarations

- Funding. The Department of Defense provided funding for some development activities under MTEC project 20-06-MOM from the Army Medical Research and Development Command. The views, opinions, and/or findings contained in this material are those of the authors and should not be interpreted as representing the official views or policies of the Department of Defense or the U.S. Government.
- Conflict of interest/Competing interests. D.S.R. and M.J.K. hold a greater than 5% equity interest in Nia Therapeutics Inc., a company intended to develop and commercialize brain stimulation therapies for memory restoration.

References

[1] Dyck, C., Swanson, C., Aisen, P., Bateman, R., Chen, C., Gee, M., Kanekiyo, M., Li, D., Reyderman, L., Cohen, S., Froelich, L., Katayama, S., Sabbagh, M., Vellas, B., Watson, D., Dhadda, S., Irizarry, M., Kramer, L.D., Iwatsubo, T.: Lecanemab in Early Alzheimer's Disease. N Engl J Med. **388**(1), 9–21 (2023) https://doi.org/10.1056/NEJMoa2212948

[2] Sims, J.R., Zimmer, J.A., Evans, C.D., Lu, M., Ardayfio, P., Sparks, J., Wessels, A.M., Shcherbinin, S., Wang, H., Monkul Nery, E.S., Collins, E.C., Solomon, P., Salloway, S., Apostolova, L.G., Hansson, O., Ritchie, C., Brooks, D.A., Mintun, M., Skovronsky, D.M., TRAILBLAZER-ALZ 2 Investigators: Donanemab in Early Symptomatic Alzheimer Disease: The TRAILBLAZER-ALZ 2 Randomized Clinical Trial. JAMA **330**(6), 512–527 (2023) https://doi.org/10.1001/jama.2023.13239

[3] Ezzyat, Y., Wanda, P.A., Levy, D.F., Kadel, A., Aka, A., Pedisich, I., Sperling, M.R., Sharan, A.D., Lega, B.C., Burks, A., Gross, R.E., Inman, C.S., Jobst, B.C., Gorenstein, M.A., Davis, K.A., Worrell, G.A., Kucewicz, M.T., Stein, J.M., Gorniak, R., Das, S.R., Rizzuto, D.S., Kahana, M.J.: Closed-loop stimulation of temporal cortex rescues functional networks and improves memory. Nature Communications **9**(1), 365 (2018) https://doi.org/10.1038/s41467-017-02753-0

[4] Kahana, M.J., Ezzyat, Y., Wanda, P.A., Solomon, E.A., Adamovich-Zeitlin, R., Lega, B.C., Jobst, B.C., Gross, R.E., Ding, K., Diaz-Arrastia, R.R.: Biomarker-guided neuromodulation aids memory in traumatic brain injury. Brain Stimulation **16**(4), 1086–1093 (2023) https://doi.org/10.1016/j.brs.2023.07.002

[5] Ezzyat, Y., Kragel, J.E., Solomon, E.A., Lega, B.C., Aronson, J.P., Jobst, B.C., Gross, R.E., Sperling, M.R., Worrell, G.A., Sheth, S.A., Wanda, P.A., Rizzuto, D.S., Kahana, M.J.: Functional and anatomical connectivity predict brain stimulation's mnemonic effects. Cerebral Cortex **34**(1), 427 (2023) https://doi.org/10.1093/cercor/bhad427

[6] Kragel, J.E., Ezzyat, Y., Sperling, M.R., Gorniak, R., Worrell, G.A., Berry, B.M., Inman, C., Lin, J.-J., Davis, K.A., Das, S.R., Stein, J.M., Jobst, B.C., Zaghloul, K.A., Sheth, S.A., Rizzuto, D.S., Kahana, M.J.: Similar patterns of neural activity predict memory function during encoding and retrieval. NeuroImage **155**, 60–71 (2017) https://doi.org/10.1016/j.neuroimage.2017.03.042

[7] Ezzyat, Y., Suthana, N.: Brain Stimulation. In: Kahana, M.J., Wagner, A.D. (eds.) Oxford Handbook of Human Memory, 2nd edn. Oxford University Press, ??? (2022)

[8] Burke, J.F., Ramayya, A.G., Kahana, M.J.: Human intracranial high-frequency activity during memory processing: neural oscillations or stochastic volatility? Current Opinion in Neurobiology **31**, 104–110 (2015) https://doi.org/10.1016/j.conb.2014.09.003

[9] Johnson, B.C., Gambini, S., Izyumin, I., Moin, A., Zhou, A., Alexandrov, G., Santacruz, S.R., Rabaey, J.M., Carmena, J.M., Muller, R.: An implantable 700W 64-channel neuromodulation IC for simultaneous recording and stimulation with rapid artifact recovery. In: 2017 Symposium on VLSI Circuits, pp. 48–49 (2017). https://doi.org/10.23919/VLSIC.2017.8008543 . https://ieeexplore.ieee.org/document/8008543

[10] Zhou, A., Santacruz, S.R., Johnson, B.C., Alexandrov, G., Moin, A., Burghardt, F.L., Rabaey, J.M., Carmena, J.M., Muller, R.: A wireless and artefact-free 128-channel neuromodulation device for closed-loop stimulation and recording in non-human primates. Nature Biomedical Engineering **3**(1), 15–26 (2019) https://doi.org/10.1038/s41551-018-0323-x

[11] Ella, A., Keller, M.: Construction of an MRI 3D high resolution sheep brain

template. Magnetic Resonance Imaging **33**(10), 1329–1337 (2015) https://doi.org/10.1016/j.mri.2015.09.001

[12] Ella, A., Delgadillo, J.A., Chemineau, P., Keller, M.: Computation of a high-resolution MRI 3D stereotaxic atlas of the sheep brain. The Journal of Comparative Neurology **525**(3), 676–692 (2017) https://doi.org/10.1002/cne.24079

[13] Rudoler, J.H., Herweg, N.A., Kahana, M.J.: Hippocampal Theta and Episodic Memory. The Journal of Neuroscience **43**(4), 613–620 (2023) https://doi.org/10.1523/JNEUROSCI.1045-22.2022

[14] Long, N.M., Kahana, M.J.: Modulation of task demands suggests that semantic processing interferes with the formation of episodic associations. Journal of Experimental Psychology. Learning, Memory, and Cognition **43**(2), 167–176 (2017) https://doi.org/10.1037/xlm0000300

[15] Mohan, U.R., Watrous, A.J., Miller, J.F., Lega, B.C., Sperling, M.R., Worrell, G.A., Gross, R.E., Zaghloul, K.A., Jobst, B.C., Davis, K.A., Sheth, S.A., Stein, J.M., Das, S.R., Gorniak, R., Wanda, P.A., Rizzuto, D.S., Kahana, M.J., Jacobs, J.: The effects of direct brain stimulation in humans depend on frequency, amplitude, and white-matter proximity. Brain Stimulation **13**(5), 1183–1195 (2020) https://doi.org/10.1016/j.brs.2020.05.009

[16] Haufe, S., Meinecke, F., Görgen, K., Dähne, S., Haynes, J.-D., Blankertz, B., Bießmann, F.: On the interpretation of weight vectors of linear models in multivariate neuroimaging. NeuroImage **87**, 96–110 (2014) https://doi.org/10.1016/j.neuroimage.2013.10.067

[17] Rajamani, N., Friedrich, H., Butenko, K., Dembek, T., Lange, F., Navrátil, P., Zvarova, P., Hollunder, B., De Bie, R.M.A., Odekerken, V.J.J., Volkmann, J., Xu, X., Ling, Z., Yao, C., Ritter, P., Neumann, W.-J., Skandalakis, G.P., Komaitis, S., Kalyvas, A., Koutsarnakis, C., Stranjalis, G., Barbe, M., Milanese, V., Fox, M.D., Kühn, A.A., Middlebrooks, E., Li, N., Reich, M., Neudorfer, C., Horn, A.: Deep brain stimulation of symptom-specific networks in Parkinson's disease. Nature Communications **15**(1), 4662 (2024) https://doi.org/10.1038/s41467-024-48731-1

[18] Sun, F.T., Morrell, M.J., Wharen, R.E.: Responsive cortical stimulation for the treatment of epilepsy. Neurotherapeutics **5**(1), 68 (2008) https://doi.org/10.1016/j.nurt.2007.10.069

[19] Holtzheimer, P.E., Kelley, M.E., Gross, R.E., Filkowski, M.M., Garlow, S.J., Barrocas, A., Wint, D., Craighead, M.C., Kozarsky, J., Chismar, R., Moreines, J.L., Mewes, K., Posse, P.R., Gutman, D.A., Mayberg, H.S.: Subcallosal cingulate deep brain stimulation for treatment-resistant unipolar and bipolar depression. Archives of General Psychiatry **69**(2), 150–158 (2012) https://doi.org/10.1001/archgenpsychiatry.2011.1456

[20] Lipsman, N., Neimat, J.S., Lozano, A.M.: Deep brain stimulation for treatment-refractory obsessive-compulsive disorder: the search for a valid target. Neurosurgery **61**(1), 1–111113 (2007) https://doi.org/10.1227/01.neu.0000279719.75403.f7

[21] Card, N.S., Wairagkar, M., Iacobacci, C., Hou, X., Singer-Clark, T., Willett, F.R., Kunz, E.M., Fan, C., Vahdati Nia, M., Deo, D.R., Srinivasan, A., Choi, E.Y., Glasser, M.F., Hochberg, L.R., Henderson, J.M., Shahlaie, K., Stavisky, S.D., Brandman, D.M.: An Accurate and Rapidly Calibrating Speech Neuroprosthesis. The New England Journal of Medicine **391**(7), 609–618 (2024) https://doi.org/10.1056/NEJMoa2314132

[22] Silva, A.B., Liu, J.R., Metzger, S.L., Bhaya-Grossman, I., Dougherty, M.E., Seaton, M.P., Littlejohn, K.T., Tu-Chan, A., Ganguly, K., Moses, D.A., Chang, E.F.: A bilingual speech neuroprosthesis driven by cortical articulatory representations shared between languages. Nature Biomedical Engineering **8**(8), 977–991 (2024) https://doi.org/10.1038/s41551-024-01207-5

[23] Sahasrabuddhe, K., Khan, A.A., Singh, A.P., Stern, T.M., Ng, Y., Tadić, A., Orel, P., LaReau, C., Pouzzner, D., Nishimura, K., Boergens, K.M., Shivakumar, S., Hopper, M.S., Kerr, B., Hanna, M.-E.S., Edgington, R.J., McNamara, I., Fell, D., Gao, P., Babaie-Fishani, A., Veijalainen, S., Klekachev, A.V., Stuckey, A.M., Luyssaert, B., Kozai, T.D.Y., Xie, C., Gilja, V., Dierickx, B., Kong, Y., Straka, M., Sohal, H.S., Angle, M.R.: The Argo: a high channel count recording system for neural recording in vivo. Journal of Neural Engineering **18**(1), 015002 (2021) https://doi.org/10.1088/1741-2552/abd0ce

[24] Brannigan, J.F.M., Fry, A., Opie, N.L., Campbell, B.C.V., Mitchell, P.J., Oxley, T.J.: Endovascular Brain-Computer Interfaces in Poststroke Paralysis. Stroke **55**(2), 474–483 (2024) https://doi.org/10.1161/STROKEAHA.123.037719

[25] Stull, S.W., Mogle, J., Bertz, J.W., Burgess-Hull, A.J., Panlilio, L.V., Lanza, S.T., Preston, K.L., Epstein, D.H.: Variability in intensively assessed mood: Systematic sources and factor structure in outpatients with opioid use disorder. Psychological Assessment **34**(10), 966–977 (2022) https://doi.org/10.1037/pas0001160

[26] Weidemann, C.T., Kragel, J.E., Lega, B.C., Worrell, G.A., Sperling, M.R., Sharan, A.D., Jobst, B.C., Khadjevand, F., Davis, K.A., Wanda, P.A., Kadel, A., Rizzuto, D.S., Kahana, M.J.: Neural activity reveals interactions between episodic and semantic memory systems during retrieval. Journal of Experimental Psychology: General **148**(1), 1–12 (2019) https://doi.org/10.1037/xge0000480

[27] Sakon, J.J., Halpern, D.J., Schonhaut, D.R., Kahana, M.J.: Human hippocampal ripples signal encoding of episodic memories. The Journal of Neuroscience, 0111232023 (2024) https://doi.org/10.1523/JNEUROSCI.0111-23.2023

[28] Rahimzadeh, V., Jones, K.M., Majumder, M.A., Kahana, M.J., Rutishauser, U.,

Williams, Z.M., Cash, S.S., Paulk, A.C., Zheng, J., Beauchamp, M.S., Collinger, J.L., Pouratian, N., McGuire, A.L., Sheth, S.A., Adolphs, R., Andersen, R.A., Baltuch, G., Brunner, P., Cash, S.S., Chang, E., Collinger, J.L., Crone, N., Fedorenko, E., Fried, I., Gold, J., Henderson, J., Hochberg, L., Howard, M., Kahana, M.J., Magnotti, J., Mamelak, A., Pouratian, N., Richardson, R.M., Rutishauser, U., Schalk, G., Schroeder, C., Shenoy, K., Sheth, S.A., Suthana, N., Tandon, N., Williams, Z.M., Wolpaw, J.: Benefits of sharing neurophysiology data from the BRAIN Initiative Research Opportunities in Humans Consortium. Neuron **111**(23), 3710–3715 (2023) https://doi.org/10.1016/j.neuron.2023.09.029

[29] Rubinstein, D.Y., Weidemann, C.T., Sperling, M.R., Kahana, M.J.: Direct brain recordings suggest a causal subsequent-memory effect. Cerebral Cortex **33**(11), 6891–6901 (2023) https://doi.org/10.1093/cercor/bhad008